Open Access Article. Published on 25 November 2022. Downloaded on 7/26/2024 12:58:23 PM.
This article is licensed under a Creative Commons Attribution-NonCommercial 3.0 Unported Licence.

RSC Advances

ROYAL SOCIETY OF CHEMISTRY

PAPER

View Article Online
View Journal | View Issue

Check for updates

Cite this: *RSC Adv.*, 2022, **12**, 33816

Dielectric property and energy storage performance enhancement for iron niobium based tungsten bronze ceramic†

Wenbin Feng, *[ab] Lilin Cheng,[a] Xiu-Ni Hua,[a] Xin Chen,[a] Hui Zhang[a]
and Haibao Duan[a]

Received 29th August 2022
Accepted 11th November 2022

DOI: 10.1039/d2ra05403e

rsc.li/rsc-advances

Ceramic dielectric capacitors have attracted increasing interest due to their wide applications in pulsed power electronic systems. Nevertheless, synchronously achieving the high energy storage density, high energy storage efficiency and good thermal stability in dielectric ceramics is still a great challenge. Herein, lead free $Sr_3SmNa_2Fe_{0.5}Nb_{9.5}O_{30}$ (SSNFN) ceramic with tetragonal tungsten bronze structure was synthesized and characterized, high total energy storage density (2.1 J cm^{-3}), recoverable energy storage density (1.7 J cm^{-3}), energy storage efficiency (80%) and good thermal stability are obtained simultaneously in the compound, due to the contribution of high maximum polarization (P_{max}), low remanent polarization (P_r) and large breakdown strength (E_b). The high P_{max} is related with the intrinsic characteristic of $Sr_4Na_2Nb_{10}O_{30}$ (SNN) based system, while the small P_r and good thermal stability stem from the significantly enhanced relaxor behavior. In addition, the large E_b originates from the improved microstructure with fewer defects and decreased average grain size, and the reduction of electrical heterogeneity compared with SNN. The capacitive performance obtained in this work points out the great potential of tungsten bronze ceramic designed for energy storage applications and pave a feasible way to develop novel lead-free dielectric capacitors.

1. Introduction

The energy storage components of pulsed power equipment, which can realize instantaneous charge and discharge processes, have become widely used in contemporary industrial fields such as hybrid electric vehicles, geological exploration, medical devices, ship propulsion systems and electromagnetic rail gun weapons. Compared with other energy storage devices, dielectric capacitors have ultra-high power density, good thermal stability, mechanical stability and excellent high voltage resistance,[1–3] which show great potential in the field of pulsed power equipment. However, because its energy storage density is far lower than that of batteries and electrochemical capacitors, it is crucial to develop dielectric energy storage materials with excellent total energy storage density (W_{total}), recoverable energy storage density (W_{rec}), and energy storage efficiency (η). Through the polarization–electric field (P–E) hysteresis curve, these three parameters can be evaluated and expressed as: $W_{total} = \int_0^{P_{max}} E\mathrm{d}P$, $W_{rec} = \int_{P_r}^{P_{max}} E\mathrm{d}P$, $\eta = \frac{W_{rec}}{W_{total}} \times 100\%$, where E, P, P_{max} and P_r indicate the applied electric field, the polarization, the maximum polarization and remanent polarization respectively.[4,5] Large P_{max}, small P_r, and high dielectric breakdown strength (E_b) are obviously important components in achieving remarkable energy storage properties. Moreover, considering the severe real working circumstances of the pulsed power equipment, the material must exhibit exceptional thermal stability for the energy storage capability.

Relaxor ferroelectric materials have great advantages in achieving high energy storage density and efficiency due to their unique nano polar micro regions, which apparently contributes to large P_{max}, slender hysteresis loop and lower P_r.[6–9] At the same time, the change of dielectric property with temperature is normally gentle for relaxor, which is conducive to obtaining relative stable dielectric permittivity, ferroelectric polarization and energy storage density in a wide temperature range.[10,11] In addition, the dynamic domain switching barrier of nano polar micro regions in relaxor ferroelectrics is lower, and the flexibility of domain wall movement can inhibit the pinning of defects, which all greatly improve the fatigue resistance and increase the service life of the materials.[6]

Tungsten bronze is one of the most important class of ferroelectrics, the cell structure is shown in the inset of Fig. 3(a) (taking the tetragonal tungsten bronze as an example). This structure provides exceptional flexibility in composition design.

---

[a] *Laboratory of Advanced Functional Materials of Nanjing, School of Environmental Science, Nanjing Xiaozhuang University, Nanjing 211171, China. E-mail: fwbnx@njxzc.edu.cn*

[b] *School of Physics, Nanjing University, Nanjing 211171, China*

† Electronic supplementary information (ESI) available. See DOI: https://doi.org/10.1039/d2ra05403e

© 2022 The Author(s). Published by the Royal Society of Chemistry

Open Access Article. Published on 25 November 2022. Downloaded on 7/26/2024 12:58:23 PM.
This article is licensed under a Creative Commons Attribution-NonCommercial 3.0 Unported Licence.

By changing the substitution and ratio of A site or B site cation filling in the crystal, the dielectric and ferroelectric properties of the material can be manipulated, and various relaxor ferroelectrics with different phase transition character can be obtained.[12–15] The openness of this structure also provides convenience for the design of dielectric capacitor energy storage materials. Moreover, recent studies have found that some tungsten bronze relaxor ferroelectrics show excellent charge–discharge performance, and their discharge rate, discharge current and power density are better than many perovskite system energy storage materials, demonstrating great potential in the field of pulsed power devices. For example, $(Ba_{0.7}Ca_{0.3})_2NaNb_5O_{15}$ has an ultra-fast discharge rate, and the discharge period $t_{0.9}$ under 120 kV cm^{-1} is only 22 ns;[16] $(Sr_{0.7}Ba_{0.3})_5LaNb_7Ti_3O_{30}$ has a discharge cycle $t_{0.9}$ of 170 ns, a power density of 61.2 MW cm^{-3}, and a discharge energy density of 2.45 J cm^{-3} at electric field of 230 kV cm^{-1};[17] $Sr_{1.88}La_{0.12}NaNb_{4.08}Ta_{0.8}Ti_{0.12}O_{15}$ has 151.1 MW cm^{-3} power density and 2.22 J cm^{-3} discharge energy density under electric field of 350 kV cm^{-1}.[18] So it is of great importance to explore tungsten bronze ceramics with outstanding comprehensive energy storage performance.

$Sr_2NaNb_5O_{15}$ ceramic is an important tungsten bronze material with high dielectric permittivity, high saturated polarization and low dielectric loss in a wide temperature range. Some studies have reported the effect of cation substitutions on energy storage property for $Sr_2NaNb_5O_{15}$, it is found that the cation substitutions can largely influence the ceramic density, the microstructure, the band gap, the dielectric loss, the polarization and E_b. These modifications mainly focus on B site substitution with Ti, Zr and Ta, and A site substitution with rare earth. It is found that the involvement of Zr or Ta in B site is beneficial to the grain refinement and band gap rising, along with dielectric constant, dielectric loss and maximum polarization decreasing.[19–22] The refinement of microstructure, the decrease of dielectric loss and increase of band gap act as the main cause for the increased breakdown strength for these compounds, and directly contribute to the improvement of energy storage density. The substitution of rare earth on A site such as La, Sm, Ho and Gd also plays positive role in enhancing the energy storage property of $Sr_2NaNb_5O_{15}$ ceramic.[22,23] However, the systematic study of energy storage property manipulation for tungsten bronzes are still very limited, considering the urgent requirement for new material in next-generation pulsed power devices, it is indispensable to explore new way to manipulate the polarization, breakdown strength and energy storage density for tungsten bronzes.

As one of the most widely distributed metal elements in nature with unique inherent character, iron is broadly involved in the research of electronic materials and the related compounds show unique magnetic, microwave absorbing and optical properties.[24–29] In perovskites, $BiFeO_3$-based ceramics show considerable potential in energy storage applications, the large leakage current and lower E_b induced by the reduction of Fe^{3+} ($Fe^{3+} + e^- \rightarrow Fe^{2+}$) can be greatly improved by chemical doping with a rare earth cation (such as La^{3+}), alkaline earth metal cation (such as Na^+ and Sr^{2+}) and transition metal cation (such as Nb^{5+}).[30–33] However, few studies have paid attention to the effect of Fe substitution on polarization, E_b and energy storage property for tungsten bronzes. In this study, the Fe based tungsten bronze ceramic is synthesized and characterized, the effect of Fe substitution in B site on crystal structure, dielectric, ferroelectric and energy storage properties, as well as the thermal stability are explored systematically. The origin of the improved energy storage property and the increased thermal stability are discussed, and this will inevitably provide important guidance for the design of new energy storage materials.

2. Experimental section

The $Sr_{4-2x}Sm_{2x}Na_2Fe_xNb_{10-x}O_{30}$ ($x = 0$, 0.5 and 1) ceramics were prepared by the conventional solid-state route. $SrCO_3$ (99.9%), Sm_2O_3 (99.99%), Na_2CO_3 (99.9%), Nb_2O_5 (99.9%), and Fe_2O_3 (99%) were utilized as raw materials and mixed in stoichiometric proportions. The powder mixture was ball milled for 6 hours using zirconia balls and ethanol. The resultant mixtures were then dried and calcined at different temperatures, the XRD patterns of them are shown in the ESI (see Fig. S1(a)–(c)†). The reaction of the raw materials to form tetragonal tungsten bronze structure occurs at different temperature for 3 hours, for example, for SNN, it happens at 1250 °C (see Fig. S1(a)†), so the calcination temperatures are 1250 °C, 1150 °C and 1100 °C respectively for $Sr_4Na_2Nb_{10}O_{30}$ (SNN), $Sr_3SmNa_2Fe_{0.5}Nb_{9.5}O_{30}$ (SSNFN) and $Sr_2Sm_2Na_2FeNb_9O_{30}$ (SSNFN1). After that the powders were re-milled and pressed into pellets 12 mm in diameter and 2 mm in thickness. They are sintered at different temperatures to obtain ceramics, the density of the ceramics are measured by the Archimedes drainage method, and the curves of density value with the change of temperature are shown in Fig. S1(d).† The sintering temperature is the temperature at which the ceramic density reaches the maximum value and the ceramic still keeps normal shape and good surface condition, so the sintering temperature are 1350 °C, 1250 °C and 1250 °C respectively for SNN, SSNFN and SSNFN1 for 3 hours.

After being polished and thermally etched at 1250 °C, 1150 °C and 1150 °C for 30 minutes respectively for SNN, SSNFN and SSNFN1, all the samples were examined using scanning electron microscopy (S-4800; Hitachi, Japan) to evaluate the microstructures. Powder X-ray diffraction (XRD) pattern was measured by a diffractometer (X'Pert PRO MPD, Panalytical, Holland) with CoKα radiation at room temperature. The dielectric properties were characterized with an LCR analyzer (Agilent 4294A, Santa Clara, CA) with a temperature-controlled cavity (VDMS 2000, Partulab, China) in the temperature range of −100 °C to 300 °C and over a frequency range of 1 kHz to 1 MHz. Silver paste was adopted as the electrodes before measurement. *P–E* hysteresis loop was identified using a ferroelectric analysis platform with temperature control system (TF analyzer 3000, aixACCT, Germany), and the gold was sputtered on the two sides of ceramics as the electrodes. The Raman spectra were evaluated by a Raman spectroscopy (HR-800 LabRama, Jobin Yvon, France) using the ceramic powders.

Open Access Article. Published on 25 November 2022. Downloaded on 7/26/2024 12:58:23 PM.
This article is licensed under a Creative Commons Attribution-NonCommercial 3.0 Unported Licence.

3. Results and discussion

Dense $Sr_4Na_2Nb_{10}O_{30}$ (SNN), $Sr_3SmNa_2Fe_{0.5}Nb_{9.5}O_{30}$ (SSNFN) and $Sr_2Sm_2Na_2FeNb_9O_{30}$ (SSNFN1) ceramics have been obtained by sintering at 1350 °C, 1250 °C and 1250 °C respectively in air for 3 hours, the density of the pellets are 4.78 g cm^{-3}, 5.12 g cm^{-3} and 5.34 g cm^{-3}, which is about 94%, 97% and 98% of the theoretical density. The dielectric permittivity (ε_r) and dielectric loss (tan δ) as a function of temperature in the range from 1 kHz to 1 MHz are shown in Fig. 1. SNN exhibits two dielectric permittivity anomalies, based on previous report, the one at about 320 °C corresponds to the transition of paraelectric phase (4/*mmm*) to ferroelectric phase (4*mm*), while the one at about −25 °C to −60 °C is related to the low temperature dielectric relaxation which exists in many tungsten bronzes due to their specific local structure disorder.[34–36] For SSNFN, the dielectric permittivity curve shows diffused nature and the maximum dielectric permittivity distributes in a wide temperature range for different frequencies, the dielectric permittivity peak value reduces and shifts to higher temperatures side with the frequency increasing, demonstrating stronger relaxor behavior of the ceramic. To get further understanding of the relaxor nature, the relationship between the dielectric permittivity peak temperature T_m and the corresponding frequency f is explored, and it follows well the Vogel–Fulcher relationship expressed as $f = f_0 \exp[-E_a/k(T_m - T_f)]$, where f is the applied ac field frequency, f_0 is the Debye frequency, E_a is the activation energy of the polar clusters, T_f is the static freezing temperature and k is the Boltzmann's constant.[37] The fitting result is shown in Fig. S2.† The data's strong agreement with the Vogel–Fulcher relationship suggests that the relaxor behavior in this material is comparable to that of a spin glass with polarization fluctuations above a static freezing point.[37,38] Compared with the dielectric property of SNN compound,[35] the maximum permittivity value of SSNFN all decreased, and the permittivity peak in the curve became increasingly broader with Fe substitution, indicating decreased polar coupling and promoted relaxor behavior. Along with this stronger relaxor nature, the thermal stability of dielectric property for the sample also improves. The flatter dielectric permittivity curve, as well as the normalized temperature-dependent dielectric constant ($(\varepsilon_r - \varepsilon_{25\ °C})/\varepsilon_{25\ °C}$) at 40 kHz shown in Fig. 1(d) all confirm this character. The thermal stability can be measured by the permittivity variation with temperature below 15%, the satisfied temperature range here is from −56 °C to 120 °C, as shown in Fig. 1(d), showing the potential for temperature stable dielectric capacitor. Meanwhile, as shown in Fig. 1(b), the dielectric loss value in the temperature range −100 to 300 °C is all less than 0.1, further confirming the thermal stability of the dielectric properties, and the low dielectric loss gives prospect for using as energy storage material with low energy loss and high energy storage efficiency. The stronger relaxor behavior of this SSNFN compound mainly originate from the Fe substitution in B site. Normally, for tungsten bronzes, Fe shows weaker displacement in BO_6 along

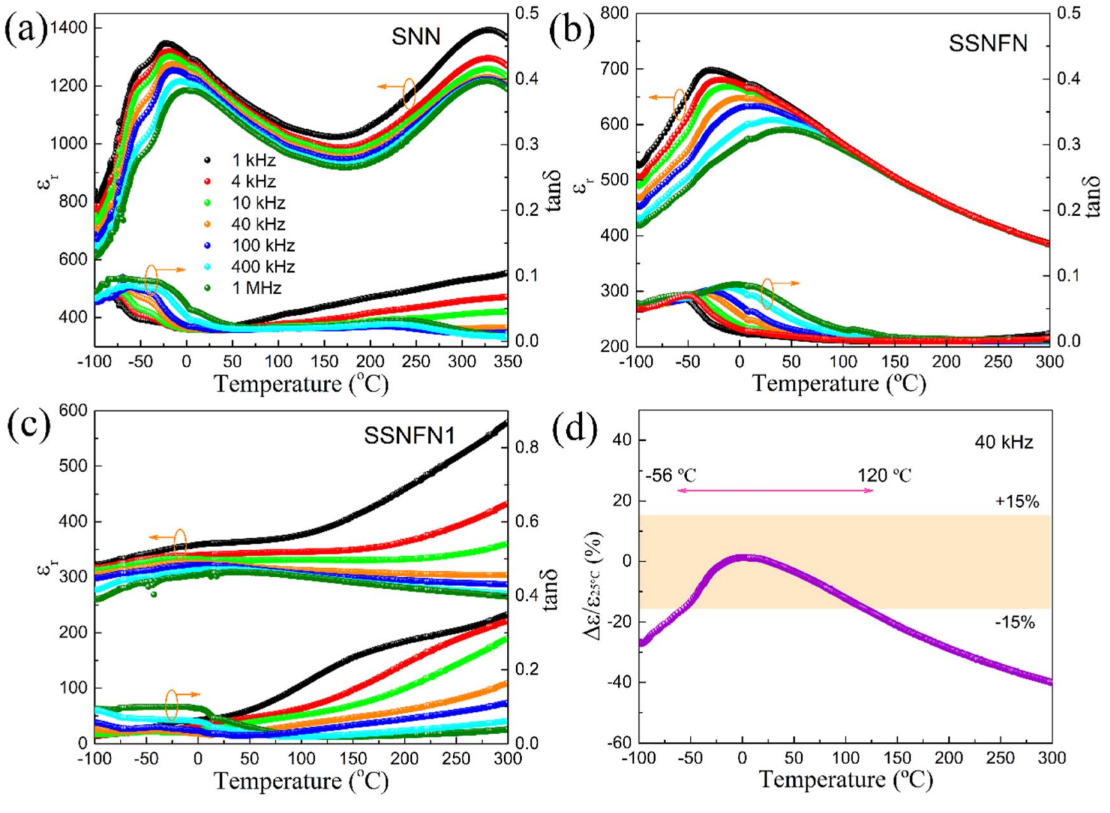

Fig. 1 Temperature dependences of dielectric permittivity ε_r and dielectric loss tan δ for (a) SNN ceramic, (b) SSNFN ceramic, and (c) SSNFN1 ceramic. (d) Evolution of $\Delta\varepsilon/\varepsilon_{25\ °C}$ ($\Delta\varepsilon = \varepsilon_r - \varepsilon_{25\ °C}$) as a function of temperature for SSNFN ceramic at 40 kHz.

© 2022 The Author(s). Published by the Royal Society of Chemistry

Open Access Article. Published on 25 November 2022. Downloaded on 7/26/2024 12:58:23 PM.
This article is licensed under a Creative Commons Attribution-NonCommercial 3.0 Unported Licence.

the polar axis, and with the Fe substitution, serious local composition, charge and lattice disorders occur for the NbO_6 matrix, it will cause disruption of the Nb–O–Nb–O long range polar order, and the disorders may also act as a source of local random field, which are all beneficial to the formation of polar nano regions.[39,40] As a result, with Fe substitution in B site, the ferroelectric transition change from normal ferroelectric to relaxor ferroelectric, the temperature of the dielectric permittivity peak largely decreases from 300 °C to −10 °C, and the two dielectric anomalies merge with each other at Fe substituted compound. For SSNFN1 ceramic whose content of Fe further increases, the dielectric permittivity anomaly almost disappears and the curve becomes quite flat, the value of both permittivity and dielectric loss exhibit sharp increase when the temperature is higher than 50 °C, which may be related to the activation of oxygen vacancies, and this indicates that the number of oxygen vacancies increases significantly for SSNFN1 compared with the SSNFN compound.

In order to explore the corresponding ferroelectric properties, the *P*–*E* hysteresis loop measured at room temperature is shown in Fig. 2. Unlike the SNN compound which exhibits saturated hysteresis loop and quite large remanent polarization, slim hysteresis loop is observed for the SSNFN compound, consistent with the stronger relaxor ferroelectric nature. The maximum polarization is 12.8 $\mu C\ cm^{-2}$, the remanent polarization is 0.8 $\mu C\ cm^{-2}$. This slim hysteresis loop reveals great advantage for obtaining large energy storage efficiency and excellent comprehensive energy storage performance for SSNFN. For SSNFN1, quite fat *P*–*E* loop is observed, indicating high energy loss under the imposed electric field and it may also have close relationship with the activation and movement of oxygen vacancies, this result is reasonable and consistent with the dielectric properties. From the above dielectric and ferroelectric measurements, it can be concluded that among the three compounds, SSNFN has a high potential for use as energy storage material.

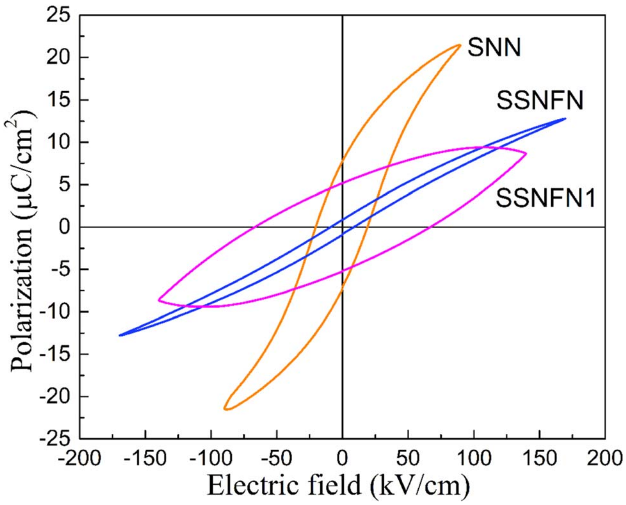

Fig. 2 Polarization–electric field (*P*–*E*) curve measured at ambient temperature with a triangular wave form at 10 Hz for SNN, SSNFN and SSNFN1 ceramics.

Fig. 3(a) shows the XRD pattern for SNN, SSNFN and SSNFN1 compounds, according to the PDF#34-0429, SNN and SSNFN were indexed as tetragonal tungsten bronze structure, there was no secondary phase observed in the substance. For SNN, Sr^{2+} substitutes the A2 sites and Na^+ substitutes the A1 sites respectively, while Nb^{5+} occupies the B1 and B2 sites. While for SSNFN, Sr^{2+} and Sm^{3+} occupies the A2 sites and Na^+ occupies the A1 sites, and Fe^{3+} and Nb^{5+} share the B1 and B2 sites together. For SSNFN1, the relative intensity of the XRD pattern is very limited although we changed the measuring condition, which may originate from its smaller particle size and relative poor crystallinity, it has tetragonal tungsten bronze structure with $NaNbO_3$ (PDF#33-1270) second phase. In the experiment, to eliminate the influence of fluorescent background of Fe due to the use of Cu target, Co target is adopted in the XRD equipment. To further investigate the correlation between local structure and property, the Raman spectra for SNN, SSNFN and SSNFN1 at room temperature are shown in Fig. 3(b). The Raman spectra of the three samples are acquired under the same measuring condition. Three distinctive internal modes (ν_1, ν_2 and ν_5) that originate from the vibration of the BO_6 octahedra, and a few external modes normally at low wave numbers that are primarily connected to the A site vibrations and the symmetry change, make up the Raman vibration modes for tungsten bronzes. The internal modes have wave numbers around 250 cm^{-1}, 630 cm^{-1}, and 845 cm^{-1}, while the bending and stretching of the BO_6 octahedral are relevant to the modes at 250 cm^{-1} and 630 cm^{-1}, and the deformation of BO_6 is relevant to the mode at 845 cm^{-1}.[41–43] For the three compounds, both the internal and external Raman modes exist, but there are some difference. First, all vibration modes are relatively broader and the FWHM of them is larger for SSNFN, such as the modes at 630 cm^{-1}, which can be seen from the figure. Normally, the increased inherent disorder of local structure accounts for this character.[43] Since the substitution of Fe in B site and Sm in A site, the degree of disorder inevitably increases. Second, the internal modes at 250 cm^{-1} and 630 cm^{-1} for SSNFN show red shift compared with SNN. The red shift of the internal mode is believed to be related to the expansion of the octahedra and the weakening of the B–O bond strength, which usually shows relaxation behavior and lower polarization intensity.[44] The red shift of Raman mode for SSNFN here is consistent with its stronger relaxor nature which has been revealed by the above experimental result. Third, Raman mode intensity of SSNFN is much smaller than SNN, although the data are collected at the same condition. According to the bond polarizability model,[45,46] the bond polarizability derivative in normal coordinate $\partial\alpha/\partial Q$ is often related to the electrons involved in the chemical bond, and it is the most significant component impacting the Raman intensity. A pure ionic bond with confined bonding electrons to a certain nucleus has a lower bond polarizability than the covalent bond. For the SSNFN and SNN compounds, considering the origin of their ferroelectricity, the difference of B–O bond plays dominant role in their local structure and property. Combining the above discussion with the experimental Raman intensity, the B–O bond covalency of SSNFN is weaker. Moreover, B–O bond with stronger covalency normally tends to form

Open Access Article. Published on 25 November 2022. Downloaded on 7/26/2024 12:58:23 PM.
This article is licensed under a Creative Commons Attribution-NonCommercial 3.0 Unported Licence.

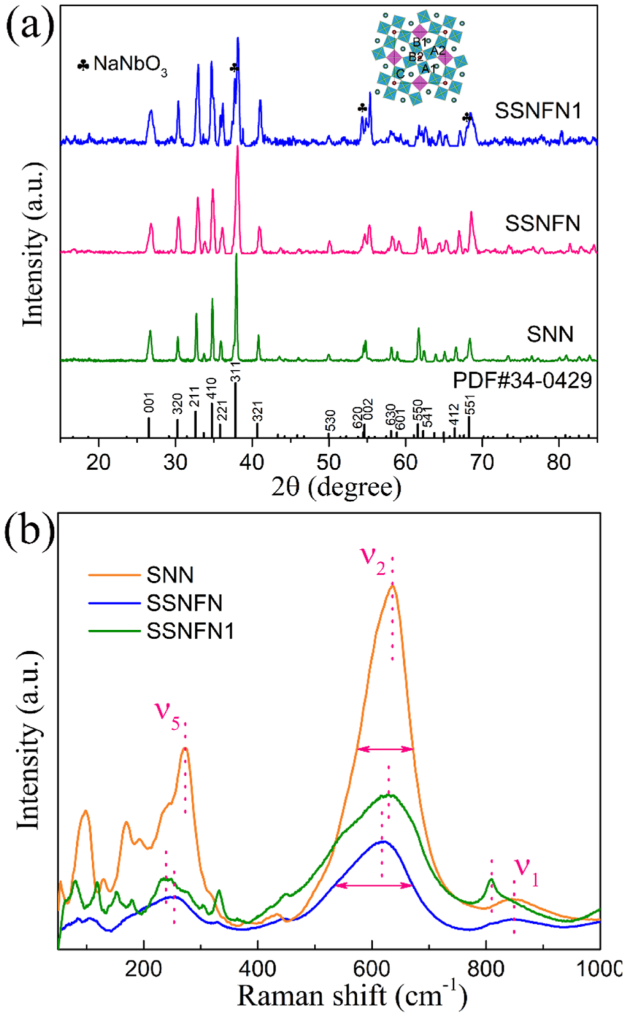

Fig. 3 (a) XRD pattern at room temperature for SNN, SSNFN and SSNFN1 ceramics. (b) Raman spectra for SNN, SSNFN and SSNFN1 ceramics at ambient temperature.

stable long-range polar order, since the Fe–O bond of SSNFN compound are less covalent and more ionic than Nb–O bond, so the long-range polar order are disrupted, consistent with the result of its relaxor behavior. For SSNFN1, internal Raman mode 630 cm^{-1} shows very slight red shift compared with SNN, while 250 cm^{-1} and 845 cm^{-1} modes exhibit strong red shift which may be related with the stronger distortion of its structure. The Raman intensity of SSNFN1 is in the middle value among these compounds, presenting the same trend of the ferroelectric polarization and it is consistent with the discussions above.

The scanning electron microscopies (SEM) of SNN, SSNFN and SSNFN1 are shown in Fig. 4, the samples show the pillar grain morphology, a sign that the cell parameter c is less than a and b. SSNFN presents a dense microstructure without appreciable pores, consistent with the high relative density. With the increase of Fe content, the average grain size becomes obviously smaller, this smaller grain size is generated as a result of the relatively low sintering temperature of them. For SSNFN, the element distribution is further investigated using the ceramic's energy dispersive spectrometer (EDS) results and elemental mapping analysis, as shown in Fig. 5. The elements in the sample are all uniformly dispersed, and the elemental ratio is compatible with the specified compound, demonstrating the production of the designed solid solution.

The high temperature complex impedance spectra of the SNN, SSNFN and SSNFN1 ceramics at 400 °C are shown in Fig. 6. The iron substituted SSNFN sample has a high resistance, excluding the effect of large scale of iron valence change at high temperature, and the larger resistance is beneficial for increasing the dielectric breakdown strength for energy storage materials. Meanwhile, the SNN ceramic has a near semi-ellipse profile, which shifts to semi-circles for SSNFN, indicating that both the grains and grain boundaries contribute to the electrical response for SNN, while grain boundaries dominate for SSNFN. This phenomena makes sense because SNN is typically difficult to synthesis and exhibits some extent of electrical heterogeneity. However, it is reported that adding additional cations in some extent to the matrix is an effective strategy to remove the microstructure and electrical heterogeneity.[6,47] The formation of a homogeneous electrical microstructure will make the electrical breakdown more difficult, thus resulting in improved E_b. The involvement of Fe and Sm in some extent in SNN matrix leads to greater resistance and electrical uniformity, which may provide favorable conditions for enhancing the E_b and energy storage density of the material. For SSNFN1, the near semi-ellipse profile is also observed, indicating that the electrical heterogeneity is also shown in the compound. This reveals that too much substitutions of Fe and Sm may lead to stronger electrical and structure inhomogeneous, which is not helpful for the improvement of energy storage properties.

To further investigate the energy storage property of the SSNFN sample, the unipolar P–E hysteresis loop is measured. Fig. 7(a) shows the room-temperature unipolar P–E curves of the

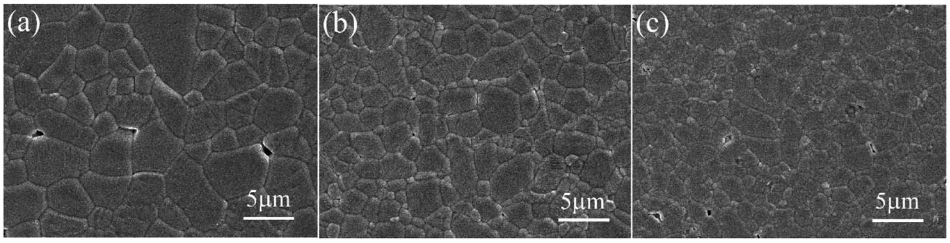

Fig. 4 SEM micrograph of SNN (a), SSNFN (b) and SSNFN1 (c) ceramics.

© 2022 The Author(s). Published by the Royal Society of Chemistry

Open Access Article. Published on 25 November 2022. Downloaded on 7/26/2024 12:58:23 PM.
This article is licensed under a Creative Commons Attribution-NonCommercial 3.0 Unported Licence.

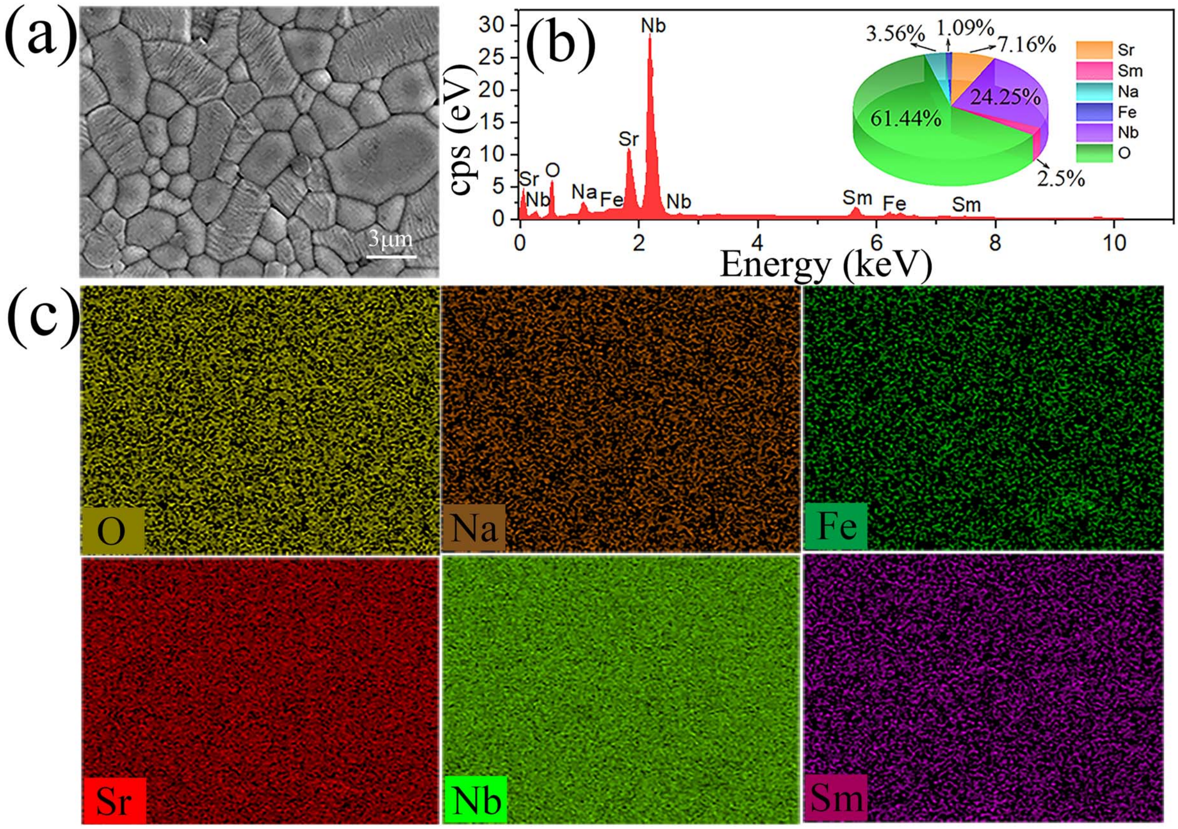

Fig. 5 SEM micrograph (a), EDS analysis result (b) and elemental mapping (c) for the SSNFN ceramic.

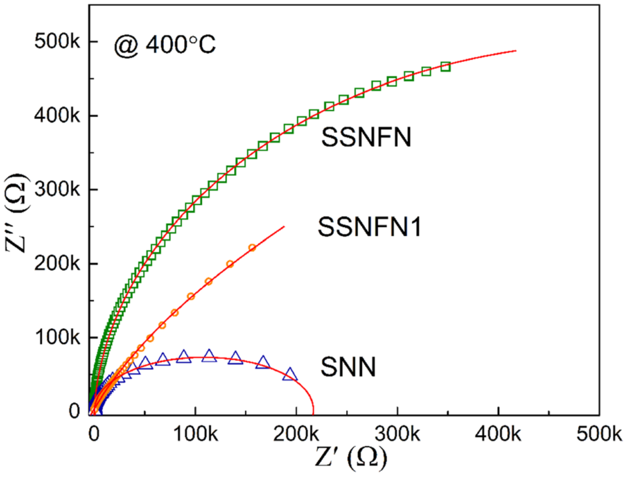

Fig. 6 Complex impedance spectrum at 400 °C for the SNN, SSNFN and SSNFN1 ceramics.

SSNFN ceramic under different electric fields at 10 Hz. All curves have a slim hysteresis loop due to the typical relaxor nature of the sample. Meanwhile, it shows outstanding voltage resistance and can reach large breakdown strength of 290 kV cm^{-1}. With the electric field increasing, the P_{max} value increases significantly with a slight improvement in P_r. As a result, larger $\Delta P(P_{max} - P_r)$ values could be obtained (as shown in the Fig. S3†), which is attributed to the formation of long range ferroelectric order induced by imposing higher external electric field. The P_{max} and ΔP reache the highest values of 15.3 μC cm^{-2} and 13.6 μC cm^{-2}, respectively, at 290 kV cm^{-1}. The energy storage properties under different electric field are also measured, as shown in Fig. 7(b). With the electric field increasing, both the total and recoverable energy storage density steadily improve, the maximum energy storage density is obtained at the maximum electric field, the total energy storage density is 2.1 J cm^{-3}, the recoverable energy storage density is 1.7 J cm^{-3}, while the energy storage efficiency remains stable under different electric field with the value of 80%, illustrating relatively excellent comprehensive energy storage performance compared with many other tungsten bronze ceramics. According to the above discussions, the enhanced dielectric breakdown strength and energy storage density of the Fe based compound are closely related to the smaller grain size, fewer defects, uniform microstructure and higher resistivity. The nature of relaxor behavior contributes to the improved energy storage efficiency for this material.

The stability of the energy storage property over broad temperature range is also evaluated. The unipolar P–E hysteresis loop is measured from room temperature to 120 °C under the imposed electric field of 150 kV cm^{-1}, as shown in Fig. 7(c). The ΔP value decreases slightly with the increasing temperature, leading to a slight decrease in W_{rec}, from 0.55 J cm^{-3} to 0.50 J cm^{-3} and a reduction in η from 79.0% to 71.2% (Fig. 7(d)). At different temperatures, the variation of total energy storage

Open Access Article. Published on 25 November 2022. Downloaded on 7/26/2024 12:58:23 PM.
This article is licensed under a Creative Commons Attribution-NonCommercial 3.0 Unported Licence.

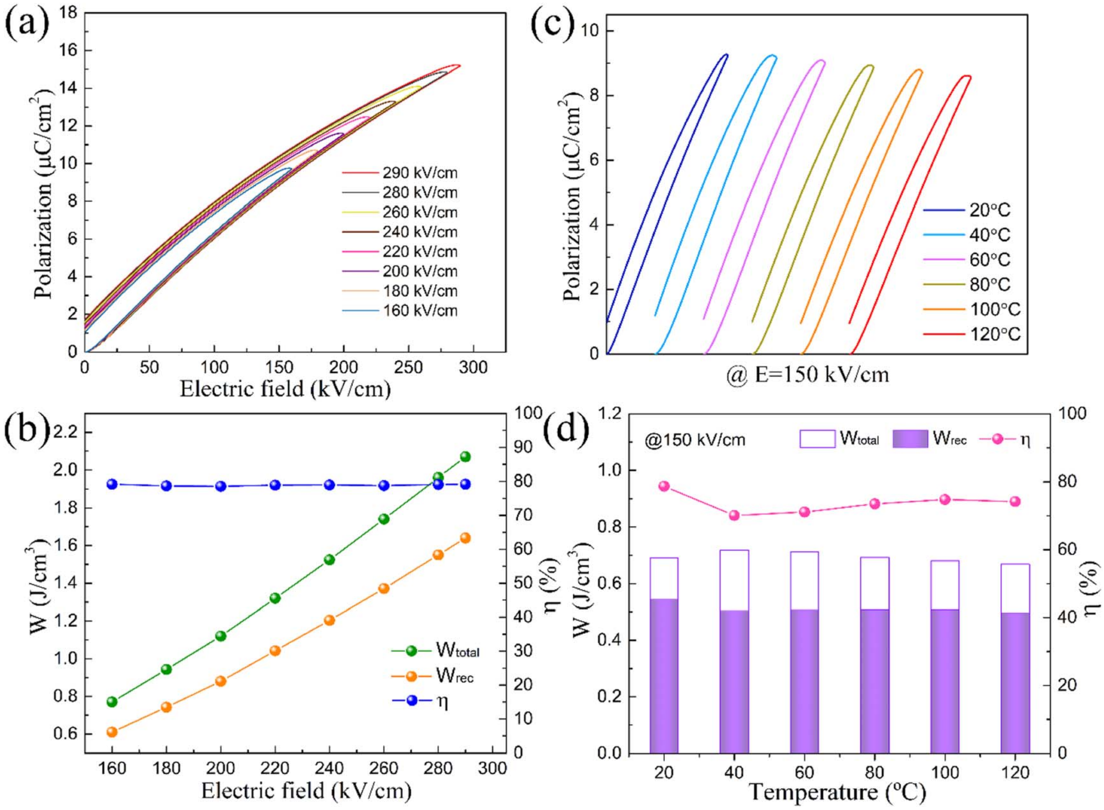

Fig. 7 Energy storage performances of the SSNFN ceramic: (a) the variation of unipolar *P*–*E* loops with increasing imposed electric field at ambient temperature; (b) the calculated total energy storage density (W_{total}), recoverable energy storage density (W_{rec}) and energy storage efficiency (η) under different electric fields at ambient temperature; (c) the temperature dependence of unipolar *P*–*E* loops from 20 to 120 °C under the electric field of 150 kV cm^{-1}; (d) the calculated W_{total}, W_{rec} and η under 150 kV cm^{-1} at different temperatures.

density, recoverable energy storage density and energy storage efficiency are less than 10%, so despite the deterioration of η at high temperatures, the SSNFN ceramic could still be utilized at a comparatively high temperature due to the reasonably stable W_{rec}. The existence of nano polar region and their insensitivity to the external stimuli are responsible for the good thermal stability of the energy storage property for the sample. In order to comprehensively evaluate its energy storage performance at different temperatures, the unipolar *P*–*E* hysteresis loops for SSNFN at 120 °C under different electric field are measured, as can be seen from Fig. S4(a) and (b),† the total and recoverable energy storage density steadily improve as the electric field increasing and the energy storage efficiency remains almost stable. The unipolar *P*–*E* hysteresis loops at 200 kV cm^{-1} at different temperatures are also measured (see Fig. S4(c) and (d)†), the SSNFN compound still shows relatively stable energy storage property. The comparison of the basic energy storage property between SSNFN and other perovskite and tungsten bronze dielectrics are shown in Table 1.[16,48–51] The relative high energy storage density, energy storage efficiency, and wide thermal stable range are simultaneously obtained in this work, illustrating its better comprehensive property and potential for energy storage dielectric capacitors.

The SSNFN ceramic exhibits high energy storage density, energy storage efficiency and thermal stability, which is closely related to its unique microstructure and electrical characteristics. Firstly, compared with other tungsten bronze systems, this compound has lower sintering temperature and higher relative

Table 1 The comparison of the basic energy storage property between the current system and other perovskite and tungsten bronze dielectrics

Composition	W_{total} (J cm^{-3})	W_{rec} (J cm^{-3})	η (%)	Stable temperature range (°C)	Ref.
$(Ba_{0.7}Ca_{0.3})_2NaNb_5O_{15}$	1.17	0.83	71	20–100	16
$0.99(0.72Bi_{0.5}Na_{0.5}TiO_3–0.28SrTiO_3)–0.01BiAlO_3$	1.75	1.24	71	40–120	48
$0.97Bi_{0.5}Na_{0.5}TiO_3–0.03BaTiO_3$	—	0.7	Less than 70	50–130	49
$0.6BiFeO_3–0.34BaTiO_3–0.06Ba(Zn_{1/3}Ta_{2/3})O_3$	3.2	2.56	80	25–85	50
$Bi_{0.5}Na_{0.5}TiO_3–SrTiO_3–0.05NaNbO_3$	1.33	0.73	55	40–160	51
$Sr_3SmNa_2Fe_{0.5}Nb_{9.5}O_{30}$	2.12	1.68	80	20–120	This work

Open Access Article. Published on 25 November 2022. Downloaded on 7/26/2024 12:58:23 PM.
This article is licensed under a Creative Commons Attribution-NonCommercial 3.0 Unported Licence.

density, as well as small grain size, few abnormal grain growth and defects such as pores and cracks, which provides favorable condition for high breakdown strength. Secondly, the compound has moderate dielectric constant, low dielectric loss and high electric resistance. According to previous studies, these characteristics are all beneficial for improving the breakdown strength and energy storage density.[6,23,30] In addition, the compound exhibits typical relaxor ferroelectric behavior, with large maximum polarization and small remanent polarization, and the change of dielectric constant and polarization value with temperature is gentle, which can ensure excellent energy storage performance and thermal stability simultaneously for the material.

4. Conclusions

In summary, lead free SSNFN ceramic with tetragonal tungsten bronze structure was synthesized and characterized for energy storage application. With the involvement of Fe cation in B site and Sm cation in A site, low sintering temperature, high relative density, uniform and compact microstructure with fine grain and fewer defects are obtained for the compound. Meanwhile, the unique dielectric and ferroelectric property of the compound, such as moderate dielectric permittivity, very low dielectric loss, strong dielectric relaxor behavior and slim hysteresis loop are beneficial for optimizing the energy storage performance. Disorder of local structure is responsible for the stronger relaxor nature and it is further confirmed through the broad Raman vibration modes and large FWHM for the modes. The increased electric resistance of the sample also contribute to enhancing the dielectric breakdown strength and energy storage density. Finally, high total energy storage density (2.1 J cm^{-3}), recoverable energy storage density (1.7 J cm^{-3}) along with high energy storage efficiency (80%) are observed for the sample simultaneously at the applied electric field of 290 kV cm^{-1}. In addition, good thermal stability of the energy storage property are also obtained. The current study paves the way for the development of new dielectric ceramics with good capacitive performance in novel tungsten bronze ceramics.

Conflicts of interest

There are no conflicts to declare.

Acknowledgements

This work was supported by National Natural Science Foundation of China under grant number 52102134, Natural Science Foundation of the Jiangsu Higher Education Institutions of China under grant number 20KJB430024 and High Level Innovative and Entrepreneurial Personnel Project of Jiangsu Province.

References

1 F. Z. Yao, Q. Yuan, Q. Wang and H. Wang, *Nanoscale*, 2020, **12**, 17165–17184.
2 Q. Li, G. Zhang, F. Liu, K. Han, M. R. Gadinski, C. Xiong and Q. Wang, *Energy Environ. Sci.*, 2015, **8**, 922–931.
3 S. Merselmiz, Z. Hanani, D. Mezzane, A. G. Razumnaya, M. Amjoud, L. Hajji, S. Terenchuk, B. Rožič, I. A. Luk'yanchukce and Z. Kutnjakf, *RSC Adv.*, 2021, **11**, 9459–9468.
4 W. B. Li, D. Zhou, R. Xu, L.-X. Pang and I. M. Reaney, *ACS Appl. Energy Mater.*, 2018, **1**, 5016–5023.
5 L. Yang, X. Kong, F. Li, H. Hao, Z. Cheng, H. Liu, J.-F. Li and S. Zhang, *Prog. Mater. Sci.*, 2019, **102**, 72–108.
6 H. Pan, F. Li, Y. Liu, Q. H. Zhang, M. Wang, S. Lan, Y. P. Zheng, J. Ma, L. Gu, Y. Shen, P. Yu, S. J. Zhang, L. Q. Chen, Y. H. Lin and C. W. Nan, *Science*, 2019, **365**, 578–582.
7 V. V. Shvartsman and D. C. Lupascu, *J. Am. Ceram. Soc.*, 2012, **95**, 1–26.
8 W. B. Li, D. Zhou and L. X. Pang, *Appl. Phys. Lett.*, 2017, **110**, 132902.
9 T. Wang, L. Jin, C. C. Li, Q. Y. Hu and X. Y. Wei, *J. Am. Ceram. Soc.*, 2015, **98**, 559–566.
10 F. T. Hu, X. F. Chen, P. Peng, F. Cao, X. L. Dong and G. S. Wang, *J. Am. Ceram. Soc.*, 2018, **101**, 4434–4440.
11 P. R. Ren, J. L. Wang, J. J. He, Y. K. Wang, H. Yuan, Y. Hao, T. Frömling, Y. H. Wan, Y. G. Shi and G. Y. Zhao, *Adv. Electron. Mater.*, 2020, **6**, 1901429.
12 L. X. Zhu, M. Fu, M. C. Stennett, P. M. Vilarinho, I. Levin, C. A. Randall, J. Gardner, F. D. Morrison and I. M. Reaney, *Chem. Mater.*, 2015, **27**, 3250–3261.
13 J. Gardner, F. J. Yu, C. Tang, W. F. Kockelmann, W. Z. Zhou and F. D. Morrison, *Chem. Mater.*, 2016, **28**, 4616–4627.
14 B. Yang, S. Hao, P. Yang, L. Wei and Z. Yang, *Ceram. Int.*, 2018, **44**, 8832–8841.
15 W. B. Feng, X. L. Zhu, X. Q. Liu and X. M. Chen, *J. Mater. Chem. C*, 2017, **5**, 4009–4016.
16 R. Li, Y. P. Pu, Q. W. Zhang, W. Wang, J. W. Li, X. Y. Du, M. Chen, X. Zhang and Z. X. Sun, *J. Eur. Ceram. Soc.*, 2020, **40**, 4509–4516.
17 L. Cao, Y. Yuan, B. Tang, E. Z. Li and S. R. Zhang, *J. Eur. Ceram. Soc.*, 2020, **40**, 2366–2374.
18 L. Cao, Y. Yuan, B. Tang, E. Z. Li and S. R. Zhang, *Chem. Eng. J.*, 2021, **421**, 127846.
19 X. Z. Zhang, H. L. Wang, X. Y. Bu, P. Zheng, L. L. Li, F. Wen, W. F. Bai, J. J. Zhang, L. Zheng, J. W. Zhai and Y. Zhang, *Inorg. Chem.*, 2021, **60**, 6559–6568.
20 M. Albino, P. Heijboer, F. Porcher, R. Decourt, P. Veber, M. Maglione and M. Josse, *J. Mater. Chem. C*, 2018, **6**, 1521–1534.
21 S. D. Xu, R. Hao, Z. Yan, S. T. Hou, Z. H. Peng, D. Wu, P. F. Liang, X. L. Chao, L. L. Wei and Z. P. Yang, *J. Eur. Ceram. Soc.*, 2022, **42**, 2781–2788.
22 X. L. Zhu, K. Y. Zhuang, S. Y. Wu and X. M. Chen, *J. Am. Ceram. Soc.*, 2018, **102**, 3438–3447.
23 L. Cao, Y. Yuan, X. Zhang, E. Li and S. Zhang, *ACS Sustainable Chem. Eng.*, 2020, **8**, 17527–17539.
24 N. Lenin, A. Karthik, S. R. Srither, M. Sridharpanday, S. Surendhiran and M. Balsubramanian, *Ceram. Int.*, 2021, **47**, 34891–34898.

© 2022 The Author(s). Published by the Royal Society of Chemistry

Open Access Article. Published on 25 November 2022. Downloaded on 7/26/2024 12:58:23 PM. This article is licensed under a Creative Commons Attribution-NonCommercial 3.0 Unported Licence.

25 P. Palaniappan, N. Lenin and R. Uvarani, *J. Mater. Sci.: Mater. Electron.*, 2022, **33**, 20293–20302.

26 P. Palaniappan, N. Lenin and R. Uvarani, *Appl. Phys. A: Mater. Sci. Process.*, 2022, **128**, 814.

27 M. Sivabharathy, S. Anu Shree, N. Lenin, B. M. Praveen, P. S. Aithal, R. Ramesh Kannan, A. Senthil Kumar and K. Ramachandran, *Mater. Today Commun.*, 2022, **33**, 104500.

28 N. Lenin, A. Karthik, M. Sridharpanday, M. Selvam, S. R. Srither, S. Arunmetha, P. Paramasivam and V. Rajendran, *J. Magn. Magn. Mater.*, 2016, **397**, 281–286.

29 P. Palaniappan, N. Lenin and R. Uvarani, *J. Alloys Compd.*, 2022, **925**, 166717.

30 T. Cui, J. Zhang, J. Guo, X. J. Li, S. Guo, Y. Huan, J. Wang and S.-T. Zhang, *J. Mater. Chem. A*, 2022, **10**, 14316–14325.

31 F. Yan, Y. Shi, X. Zhou, K. Zhu, B. Shen and J. Zhai, *Chem. Eng. J.*, 2021, **417**, 127945.

32 H. Yang, H. Qi and R. Zuo, *J. Eur. Ceram. Soc.*, 2019, **39**, 2673–2679.

33 Z. Lu, G. Wang, W. Bao, J. Li, L. Li, A. Mostaed, H. Yang, H. Ji, D. Li, A. Feteira, F. Xu, D. C. Sinclair, D. Wang, S.-Y. Liu and I. M. Reaney, *Energy Environ. Sci.*, 2020, **13**, 2938–2948.

34 A. Torres-Pardo, R. Jiménez, J. M. González-Calbet and E. García-González, *Inorg. Chem.*, 2011, **50**, 12091–12098.

35 L. L. Wei, Z. P. Yang, R. Gu and H. M. Ren, *J. Am. Ceram. Soc.*, 2010, **93**, 1978–1983.

36 E. García-González, A. Torres-Pardo, R. Jiménez and J. M. González-Calbet, *Chem. Mater.*, 2007, **19**, 3575–3580.

37 D. Viehland, S. J. Jang, L. E. Cross and M. Wuttig, *J. Appl. Phys.*, 1990, **68**, 2916–2921.

38 L. E. Cross, *Ferroelectrics*, 1987, **76**, 241–267.

39 T. T. Gao, W. Chen, X. N. Zhu, X. L. Zhu and X. M. Chen, *Mater. Chem. Phys.*, 2016, **181**, 47–53.

40 E. E. McCabe and A. R. West, *J. Solid State Chem.*, 2010, **183**, 624–630.

41 J. L. B. Faria, P. T. C. Freire, A. P. Ayala, F. E. A. Melo, J. Mendes Filho, C. W. A. Paschoal, I. A. Santos and J. A. Eiras, *J. Raman Spectrosc.*, 2003, **34**, 826–830.

42 V. Massarotti, D. Capsoni, M. Bini, C. B. Azzoni, M. C. Mozzati and P. Galinetto, *J. Phys. Chem. C*, 2007, **111**, 6857–6861.

43 J. J. Lima-Silva, D. Garcia, J. Mendes Filho, J. A. Eiras and A. P. Ayala, *Phys. Status Solidi B*, 2004, **241**, 2001–2006.

44 L. Cao, Y. Yuan, X. J. Meng, E. Z. Li and B. Tang, *ACS Appl. Mater. Interfaces*, 2022, **14**, 9318–9329.

45 L. A. Woodward and D. A. Long, *Trans. Faraday Soc.*, 1949, **45**, 1131–1141.

46 J. Tang and A. C. Albrecht, *J. Chem. Phys.*, 1968, **49**, 1144–1154.

47 G. Wang, J. Li, X. Zhang, Z. Fan, F. Yang, A. Feteira, D. Zhou, D. C. Sinclair, T. Ma, X. Tan, D. Wang and I. M. Reaney, *Energy Environ. Sci.*, 2019, **12**, 582–588.

48 P. Shi, L. Zhu, W. Gao, Z. Yu, X. Lou, X. Wang, Z. Yang and S. Yang, *J. Alloys Compd.*, 2019, **784**, 788–793.

49 Q. Li, J. Wang, Y. Ma, L. Ma, G. Dong and H. Fan, *J. Alloys Compd.*, 2016, **663**, 701–707.

50 N. Liu, R. Liang, Z. Zhou and X. Dong, *J. Mater. Chem. C*, 2018, **6**, 10211–10217.

51 F. Li, J. Zhai, B. Shen, X. Liu, K. Yang, Y. Zhang, P. Li, B. Liu and H. Zeng, *J. Appl. Phys.*, 2017, **121**, 054103.

© 2022 The Author(s). Published by the Royal Society of Chemistry